

Characterizing Precipitation Behaviors of H^- in the Martian Atmosphere

Sarah Henderson^{1,2}, Jasper Halekas¹, Rebecca Jolitz³, David Mitchell³,
Christian Mazelle⁴, Frank Eparvier⁵, Meredith Elrod^{6,7}

¹The University of Iowa, Iowa City, IA, USA

²Montana State University, Bozeman, MT, USA

³Space Sciences Laboratory, University of California Berkeley, Berkeley, CA, USA

⁴IRAP, Université de Toulouse, CNRS, UPS, CNES, Toulouse, France

⁵Laboratory for Atmospheric and Space Physics, University of Colorado, Boulder, CO, USA

⁶Planetary Environments Lab, Goddard Space Flight Center, NASA, Greenbelt, MD, USA

⁷CRESST II, University of Maryland, College Park, College Park, MD, USA

Key Points:

- H^- precipitation events at Mars occur primarily during high energy solar wind events during perihelion
- H^- fluxes are on average 4.5 times less than those of H^+ , indicating preferential conversion of energetic neutral atoms to H^+
- Effects of photodetachment on H^- are notable at ionospheric altitudes above 125 km

Corresponding author: Sarah Henderson, sarah.henderson5@montana.edu

Abstract

Solar wind protons can charge exchange with the extensive hydrogen corona of Mars, resulting in a significant flux of energetic neutral atoms (ENAs). As these solar wind hydrogen ENAs precipitate into the upper atmosphere, they can experience electron attachment or detachment, resulting in populations of H^- and H^+ , respectively, with upstream velocity. We seek to characterize the behavior of H^- in the ionosphere of Mars through a combination of in situ data analysis and mathematical models. Observations indicate that measurable H^- precipitation in the ionosphere of Mars is rare, occurring during only 1.8% of available observations. These events occur primarily during high energy solar wind conditions near perihelion. We also compare H^- fluxes to those of H^+ and find that H^- fluxes are ~ 4.5 times less than H^+ , indicating preferential conversion of hydrogen ENAs to H^+ . We develop a simple model describing the evolution of the charged and neutral fraction of ENAs and H^- ions versus altitude. We find that 0.29 - 0.78% of ENAs are converted to H^- for solar wind energies 1 - 3 keV. We also predict that the effects of photodetachment on the $\text{H}-\text{H}^-$ system are non-negligible.

Plain Language Summary

As the solar wind propagates throughout the solar system, it can directly interact with the atmosphere of Mars. Protons in the solar wind can obtain an electron from hydrogen in the planet's large atmosphere, resulting in a population of energetic neutral hydrogen atoms (ENAs). These ENAs bypass electromagnetic boundaries, penetrating into the collisional CO_2 component of the Martian atmosphere. Through interactions with CO_2 , these ENAs can obtain or lose an electron, generating populations of H^- and H^+ . We find that observing measurable amounts of H^- at Mars is rather difficult. These ions are best observed during high energy solar wind conditions during Mars's closest approach to the Sun. We also find that hydrogen ENAs are more often converted to H^+ than H^- . We also develop a simple mathematical model describing how many ENAs are converted to H^- . We find that in addition to collisional interactions with CO_2 , interactions between solar radiation and H^- are non-negligible. We determine that a minute fraction of ENAs are converted to H^- .

1 Introduction

Mars is home to both a collisional CO_2 dominated atmosphere and an extensive hydrogen corona (Anderson Jr., 1974; Chaufray et al., 2008). As the solar wind propagates towards Mars, protons within the solar wind directly interact with hydrogen atoms within the planet's corona. These protons can charge exchange with neutral hydrogen, becoming energetic neutral atoms (ENAs) with upstream solar wind energies (Gunell et al., 2006; Holmström et al., 2002; Kallio et al., 1997). These ENAs bypass electromagnetic boundaries about Mars and penetrate to altitudes of ~ 120 km. Along their path of propagation, these ENAs undergo three primary mechanisms: electron stripping, electron attachment, or excitation. These processes result in measurable populations of H^+ (Kallio & Barabash, 2001; Halekas et al., 2015), H^- (Halekas et al., 2015), and proton aurora (Deighan et al., 2018; Ritter et al., 2018).

Previous studies have explored numerous characteristics of this ENA population and its various byproducts in the atmosphere of Mars using in situ data (Brinkfeldt et al., 2006; Futaana et al., 2006a, 2006b; Gunell et al., 2006; Wang et al., 2013; Halekas et al., 2015; Halekas, 2017; Halekas et al., 2017; Deighan et al., 2018; Hughes et al., 2019; Henderson et al., 2021, 2022; Jones et al., 2022) as well as modeling techniques (Brecht, 1997; Kallio et al., 1997; Kallio & Barabash, 2001; Holmström et al., 2002; Kallio et al., 2006; V. I. Shematovich et al., 2011; Diéval et al., 2012; Wang et al., 2013; Bisikalo et al., 2018; Wang et al., 2018; V. Shematovich & Bisikalo, 2021; Hughes et al., 2023). More recent studies have focused on the behaviors of the charged byproducts of this popula-

tion (H^+ and H^-) as a function of various spatial and temporal parameters (Halekas, 2017; Henderson et al., 2021, 2022; Jones et al., 2022).

The properties of H^- , in particular, have been left largely unexplored. One previous study examined how these particles' fluxes vary with respect to season, upstream solar wind energy, and how H^- densities compare to upstream solar wind protons and penetrating H^+ (Jones et al., 2022). In this manuscript, we seek to focus on the behaviors of H^- in the Martian atmosphere using a combination of in situ data and mathematical models. We examine data collected by the Mars Atmosphere and Volatile Evolution (MAVEN) spacecraft to determine under what conditions H^- is most often observed at Mars (Jakosky et al., 2015). We cross-compare the observed fluxes of H^- and H^+ as a function of atmospheric CO_2 column density. We then use a previous framework outlined in Halekas (2017) describing the evolution of the charge fraction of H^+ as a function of altitude to discuss the anticipated equilibrium behaviors of H^- . We develop a simple model describing the neutral and negative charge fractions of hydrogen ENAs and H^- by examining the effects of charge exchange, electron attachment, and photodetachment. Finally, we compare our modelling results to our data set.

2 H^- In Situ Observations

Before modeling the behavior of H^- , we are interested in characterizing how these particles behave in the Mars atmosphere by utilizing in situ data. We focus on isolating MAVEN observations where H^- and H^+ ions are present. The following sections describe how we obtain the H^- data, as well as under what conditions we most frequently observe this particle population. We also briefly compare how H^- and H^+ fluxes vary with respect to CO_2 column density.

2.1 Methodology

We begin by examining Solar Wind Ion Analyzer (SWIA) and Solar Wind Electron Analyzer (SWEA) L2 archive data collected during MAVEN dayside periapses at altitudes below 250 km between 2014 and 2023 (Halekas et al., 2015; D. Mitchell et al., 2016).

For each orbit, we determine if the Sun is within SWEA's and/or SWIA's field of view (FOV). Due to the position of both instruments on MAVEN in addition to the spacecraft's orbital configuration, the Sun may not necessarily be within the instruments' FOVs during each periapsis (Halekas et al., 2015; D. Mitchell et al., 2016). Depending on the orbital configuration, the Sun may only be observable by one of the instruments. In order to best detect both H^+ and H^- , it is critical that the instruments are pointed sunward since solar wind hydrogen ENAs are highly collimated in the antisunward direction. Once we confirm that the Sun is in the relevant instrument's FOV, we proceed to analyze the electron and ion data collected within that periapsis.

Due to low count statistics, we first determine an average background count rate for each orbit. We separate the electron data into backscattered and downward populations using the same methods described in Girazian and Halekas (2021). Namely, we determine the dot product between the electron's velocity vector and Mars surface normal for a given measurement. If the dot product is positive, this is considered backscattered; the opposite is true for the downward condition (Girazian & Halekas, 2021). Due to SWEA's position on MAVEN, specific anode bins are physically blocked by the spacecraft; we therefore exclude these bins from our analysis within the downward and backscattered data (D. Mitchell et al., 2016). Once these anodes are masked, we compute an angular sum to generate an energy-count profile for a given timestamp and repeat this process for each individual 8-second observation during a periapsis. We also implement an outlier rejection to the SWEA data to better isolate the H^- signal. It has been shown

118 that magnetosheath electrons are able to precipitate into the upper Martian atmosphere
119 under certain magnetic field configurations, resulting in “hot” electron signatures vis-
120 ible below altitudes of 250 km (D. L. Mitchell et al., 2001). To mitigate this, we sum the
121 electron counts for energies above 600 eV in each time bin collected over a periapsis for
122 both the backscattered and downward populations. Once we obtain total counts per time
123 stamp in each direction, we find the median total counts for a given periapsis in each re-
124 spective direction. Any timestamps where the total counts exceed 2.5 times the periap-
125 sis median is rejected. This threshold was chosen empirically after examining a multi-
126 tude of periapses. We then proceed to sum over all timestamps for the duration of the
127 periapsis for the backscattered data, resulting in an angular-averaged count-energy pro-
128 file. From this total backscattered profile, we take the average number of counts in the
129 three highest energy bins to generate an average background for a given periapsis.

130 Once this average background is obtained from the backscattered data, we turn to
131 the downward propagating data. The main purpose of obtaining the background for each
132 periapsis is two-fold: to determine whether the total H^- signal is statistically significant
133 compared to that of the background and to perform a background subtraction. To de-
134 termine if the H^- signal is significantly different from that of the background (BG), we
135 first isolate the total core counts (C_{core}) that are collected at energies within $0.83E_{SW}$
136 $\leq E_{SW} \leq 1.34E_{SW}$, where E_{SW} is the upstream solar wind energy for that particular
137 orbit. This range of energies was chosen in order to encompass neighboring energy bins
138 for SWEA, given that the instrument’s resolution is 17% (D. Mitchell et al., 2016). We
139 tailor this limit towards higher energies in order to prevent signals from low energy sources
140 (i.e., Auger electrons) from dominating our signal.

141 We repeat these methods on the SWIA H^+ data with two subtle changes. For the
142 hot population filter, we sum over energies above 200 eV; this range is imposed in or-
143 der to eliminate potential spacecraft charging signatures while still detecting planetary
144 ion populations or accelerated heavy ions (Halekas et al., 2017). The second change that
145 we implement is the range of energies we examine in order to isolate each distribution’s
146 core points. We focus on energy bins that satisfy $0.855E_{SW} \leq E_{SW} \leq 1.29E_{SW}$; these
147 limits were chosen due to SWIA’s intrinsic resolution of 14.5% (Halekas et al., 2015).

148 Once we remove hot populations in both the H^- and H^+ data, we then compare
149 the distribution of isolated core counts to the background counts of each population’s
150 signal. To do so, we compute a z-score using a right-tailed Z test,

$$151 \quad z = \frac{\overline{C_{core}} - \overline{BG}}{\sqrt{(\sigma_{core}/\sqrt{N_{core}})^2 + (\sigma_{BG}/\sqrt{N_{BG}})^2}}, \quad (1)$$

152 where $\overline{C_{core}}$ is the average of the isolated core points, \overline{BG} is the average of the background
153 counts, σ_{core} is the standard deviation of the core counts, σ_{BG} is the standard deviation
154 of the background counts, N_{core} is the number of core counts, and N_{BG} is the number
155 of background counts. Note that these standard deviations are computed using Bessel’s
156 correction to account for bias in small population samples. We ultimately convert these
157 z-scores into a more familiar p-value using a right-tailed test lookup table.

158 In addition to computing a z-score, we also compute a signal to noise ratio (SNR)
159 for each periapsis. We implement this statistic as well after examining the distribution
160 of p-scores for the H^- signals. To compute a SNR, we compare the core counts to those
161 of the background. We find the peak total number of counts in the core of the distribu-
162 tion and take the ratio of this and the average background counts. After examining var-
163 ious orbits, we determine that a $SNR \geq 3$ quantifies a statistically significant signal.

164 After repeating the above process for H^- and H^+ data, we conclude that further
165 visual confirmation is needed to determine if an H^- signal is actually present. Figure 2
166 shows the distribution of SNRs and p-scores for the dayside orbits between 2014 and 2023
167 where data were available for SWEA and/or SWIA. We see a clear difference between

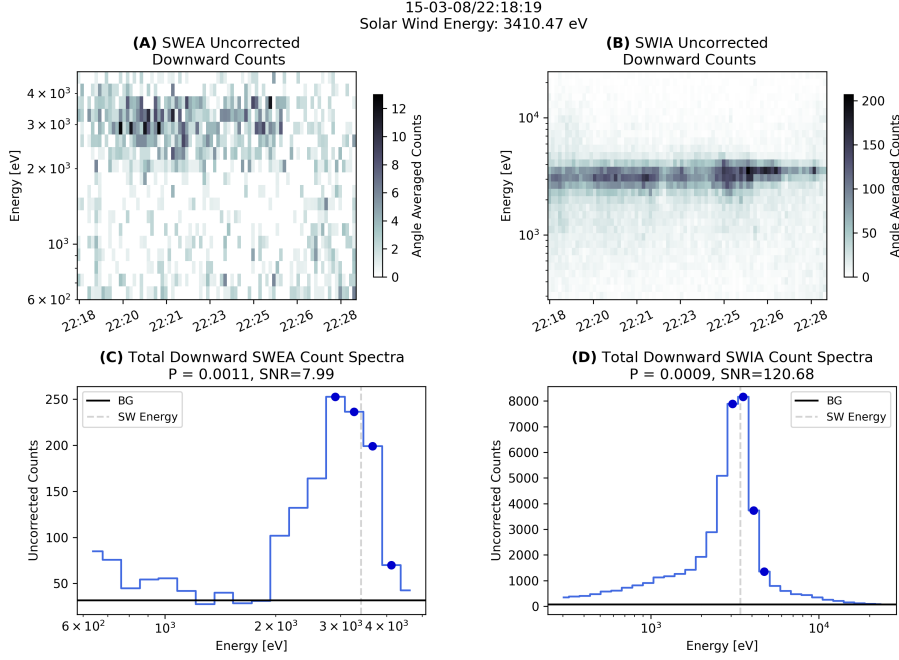


Figure 1. Example of SWEA and SWIA uncorrected count-energy spectra from a coronal mass ejection event on March 8, 2015. (A) Downward, angle summed count profile for SWEA without background correction. (B) Same as Panel A, but for SWIA. (C) Coadded SWEA orbital profile resulting from summing over all timestamps in Panel A. Blue points represent C_{core} . (D) Same as Panel C, but for SWIA. Note different scaling on each subpanel.

168 the two datasets; SWIA H^+ data are significantly more robust than SWEA H^- data.
 169 Of the 2,344 SWEA observations available, 1,708 (72.9%) had background levels that
 170 were higher than the core counts. Of SWIA's 4,247 available observations, only 186 (4.38%)
 171 demonstrated this behavior. When examining the distribution of orbits that satisfy what
 172 we deem as a statistically significant threshold ($SNR \geq 3$ and $p \leq 0.05$), we are left with
 173 68 SWEA orbits and 2,761 SWIA orbits. Upon further inspection of numerous orbits,
 174 we find that the backscattered signal detected by SWEA in its highest energy bins is some-
 175 times higher than anticipated. This skews the p-score and SNR to values outside of what
 176 we would nominally deem statistically significant, even if an H^- signal is indeed present.
 177 We also find that during orbits with upstream solar wind energy less than ~ 1000 eV,
 178 the p-score and SNR are often skewed towards more statistically significant values due
 179 to high signals of Auger electrons contaminating the region where we anticipate H^- to
 180 be present. Because of these factors, we examine all available orbits by eye to determine
 181 if a signal is detected, an example of which can be seen in Figure 1. Once we visually
 182 confirm that an H^- signal is present within a given periapsis, we proceed to analyze each
 183 8-second or 4-second slice of downward propagating H^- and H^+ data, respectively.

184 We compute an average background count rate for a given periapsis by dividing
 185 \overline{BG} by the duration of the periapsis in seconds. We then apply a background correction
 186 to each energy-anode bin using this background count rate to try and eliminate instru-
 187 ment background and counts generated by high energy particles, such as cosmic rays.
 188 After applying this correction, we convert these background corrected counts into dif-
 189 ferential energy flux. We then sum over all anode bins to generate an angular-averaged
 190 profile for the downward population observed during each individual timestamp. This

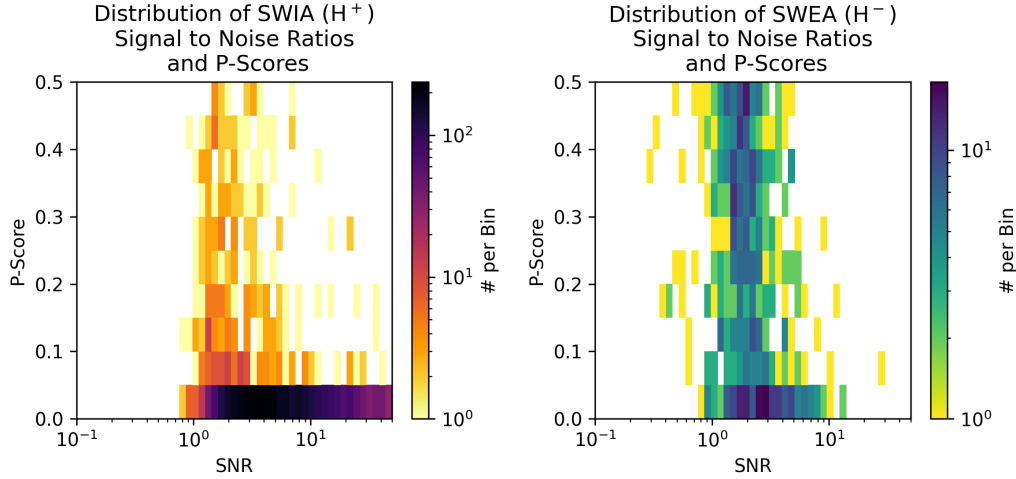


Figure 2. Distribution of p-scores and signal to noise ratios (SNRs) for SWIA and SWEA dayside periapses between 2014 and 2023. Note different scaling on colorbars.

191 process is repeated for both SWEA and SWIA data at an 8-second or 4-second cadence,
 192 respectively.

193 With the aforementioned energy restrictions, FOV constraints, L2 archive data avail-
 194 ability, and visual confirmation, we are only left with 43 periapses to cross compare H^+
 195 and H^- .

196 2.2 Results

197 We seek to compare the behavior of H^+ and H^- in the Martian atmosphere by ex-
 198 amining temporal and spatial characteristics of their energy spectra. As is apparent from
 199 Figure 1, the flux of H^- is significantly lower than that of H^+ and other ion species within
 200 the Martian ionosphere. Particularly, the backscattered signal of H^- is extremely dimin-
 201 ished; we therefore only examine downward propagating populations of H^+ and H^- in
 202 this analysis.

203 2.2.1 Distribution of H^- Detections

204 Since detection of H^- events is rare (1.8% of available orbits), we first want to de-
 205 termine under what conditions these particles are most frequently observed. Figure 3
 206 summarizes the distribution of these orbits as a function of various relevant parameters.

207 We see a clear bias towards H^- events occurring near perihelion ($L_S=251^\circ$) and
 208 during southern summer ($270^\circ \leq L_S \leq 360^\circ$). This is not surprising, given the seasonal
 209 increase in the exposed hydrogen column density upstream of the Martian bow shock,
 210 which allows for an increased rate of ENA generation and consequent charge-changing
 211 processes (Halekas, 2017). Additionally, dust season occurs within southern summer; dust
 212 storms have been shown to sweep up water molecules to ionospheric altitudes, where they
 213 can undergo photodissociation (Chaffin et al., 2021). This process creates a larger source
 214 of hydrogen within the upper atmosphere of Mars, which may also aid in the creation
 215 of more H^- ions. In conjunction with a seasonal bias, we also observe a higher occur-
 216 rence of H^- precipitation events for high solar wind energies. We would also anticipate
 217 this trend for two reasons: an increased cross section of interaction and easier discern-

Distribution of H^- Orbital Detections

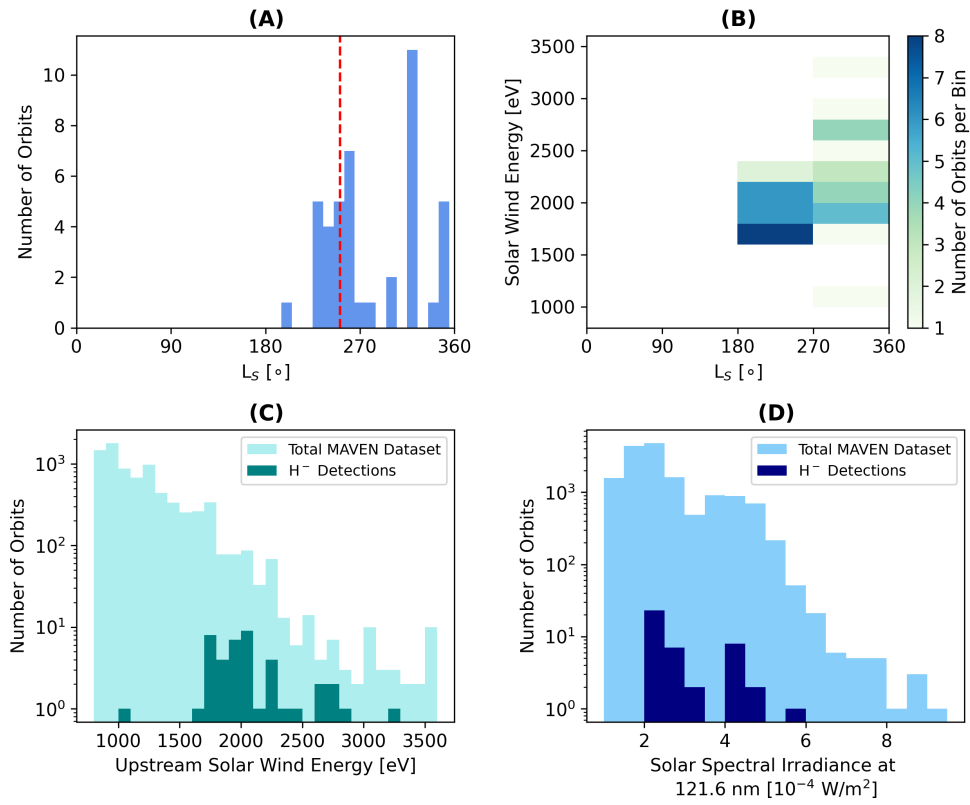


Figure 3. Distribution of orbits with H^- detections with respect to solar longitude (L_S), solar wind energy, and solar EUV irradiance. Red vertical line in Panel A indicates perihelion ($L_S = 251^\circ$).

218 ment from other electron populations at Mars. The cross section for electron attachment
 219 increases significantly with increasing solar wind energy (Lindsay et al., 2005). Addition-
 220 ally, Auger and/or photoelectrons are not present at these higher energies, which also
 221 allows us to see H^- precipitation much more clearly.

222 Another potentially important factor affecting H^- precipitation is solar extreme
 223 ultraviolet (EUV) emission. Utilizing orbit-averaged L2 data from the Extreme Ultra-
 224 violet Monitor (EUVM) onboard MAVEN, we examine the distribution of H^- events as
 225 a function of solar Lyman- α emission (Eparvier et al., 2015). In Figure 3 Panels B and
 226 D, we do not see any strong correlation between H^- precipitation and solar EUV irra-
 227 diance. Compared to the overall distribution of solar EUV irradiance measurements col-
 228 lected over the duration of the MAVEN mission, we do not see any particular bias in H^-
 229 detections towards high or low periods of solar flux. This indicates that H^- precipita-
 230 tion should occur throughout various points of the solar cycle, which is indeed what we
 231 observe in Figure 4.

232 From Figure 4A, we see that the majority of H^- detections are clustered in 2016
 233 near perihelion during the declining phase of Solar Cycle 24. We also observe a second
 234 cluster of events in 2022 as we approach Solar Cycle 25 maximum, where the solar EUV
 235 input is ~ 2 -3 times larger than during solar minimum. This distribution of events in-
 236 dicates that there is no strong correlation between solar cycle and observed H^- precip-
 237 itation. Figure 4B summarizes the distribution of events as a function of solar EUV ir-
 238 radiance as well as solar wind energy. We see from this panel that events occurring dur-
 239 ing periods of lower EUV input are observed at a broader range of energies when com-
 240 pared to those that occur near solar maximum.

241 We also see in Figure 4A that all events prior to 2022 are primarily clustered near
 242 perihelion. This can most likely be attributed to the seasonal variability of the hydro-
 243 gen corona; at perihelion, the exposed hydrogen column density upstream of the bow shock
 244 increases by a factor of ~ 3 compared to aphelion (Halekas, 2017). Having more hydro-
 245 gen available upstream of the bow shock allows for a higher production rate of ENAs (up
 246 to $\sim 5\%$), which ultimately allows for a higher likelihood of H^- and H^+ precipitation (Halekas,
 247 2017).

248 The trends presented in Figures 3 and 4 seem to indicate that there is a “sweet-
 249 spot” for H^- precipitation in the upper atmosphere of Mars. We observe a bias in H^-
 250 precipitation events during high energy solar wind conditions, which often coincide with
 251 heightened periods of solar activity. We also observe most precipitation events near per-
 252 ihelion, where both the solar EUV irradiance and the amount of exposed hydrogen col-
 253 umn density upstream of Mars’s bow shock peak in the planet’s orbit about the Sun. Shortly
 254 after perihelion, we observe an uptick in H^- precipitation events during southern sum-
 255 mer solstice, which coincides with Mars’s dust season. We also observe precipitation events
 256 at various points within the solar cycle, suggesting there is not a strong dependence of
 257 H^- precipitation on solar EUV emission. With all of these factors, it appears that there
 258 are a multitude of drivers that affect H^- precipitation. Our findings suggest a delicate
 259 balance between solar wind conditions, solar activity, and Martian atmospheric condi-
 260 tions is required in order to observe H^- . Further observations are required to better un-
 261 derstand the behaviors presented here.

262 *2.2.2 Column Density Variation*

263 In addition to examining the distribution of H^- precipitation events, we also want
 264 to investigate the behavior of H^- and H^+ congruently as a function of atmospheric CO_2
 265 column density. Using CO_2 data from the Neutral Gas and Ion Mass Spectrometer (NGIMS),
 266 we compute column density values for each 8-second SWEA and 4-second SWIA mea-
 267 surement within our 43 orbit sample (P. Mahaffy et al., 2015). To obtain each column
 268 density value, we trace the path of the precipitating solar wind hydrogen from the Sun

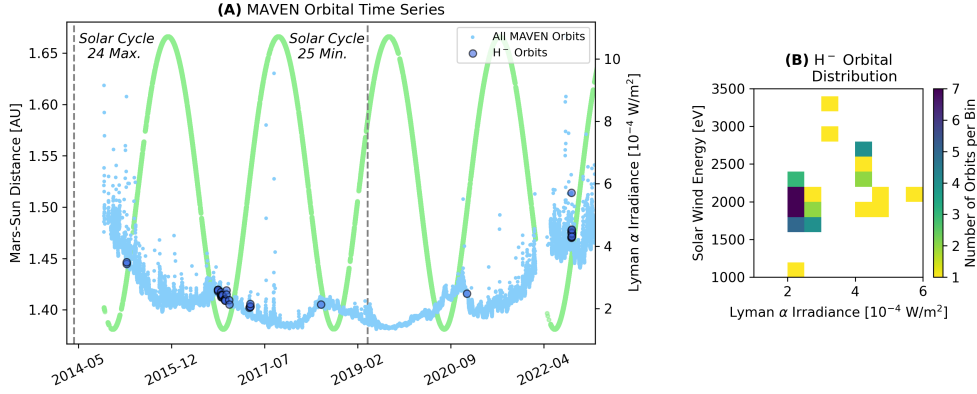


Figure 4. (A) Time series of orbit-averaged solar EUV irradiance from MAVEN Extreme Ultraviolet Monitor (EUVM) observations. Light blue points represent all orbit-averaged solar EUV irradiances, while dark blue points represent orbits where H⁻ was detected. Green points show the Mars-Sun distance in astronomical units, with the corresponding axis on the left-hand side of the figure. Solar cycle phases are indicated by the text and gray hashed lines. (B) Distribution of H⁻ orbits as a function of upstream solar wind energy and solar EUV irradiance. Note: The gap in data near April 2022 is due to MAVEN going into safe-mode.

269 to the point at which it is observed by MAVEN. Ultimately, this quantifies the amount
 270 of CO₂ that a given particle has passed through along its path of propagation. The ex-
 271 act details of this calculation are described in Henderson et al. (2021).

272 Previous studies have demonstrated that H⁺ flux varies as a function of column
 273 density, increasing as hydrogen ENAs interact with more CO₂ molecules along their path
 274 of propagation. This behavior is exhibited up until a critical column density, where H⁺
 275 and H production reach an equilibrium; ultimately, a “turnover” in the flux profile is ob-
 276 served where collisional processes and consequential energy loss dominate (Halekas, 2017;
 277 Henderson et al., 2021). We anticipate a similar behavior demonstrated by H⁻; however,
 278 the point at which this turnover occurs may vary due to different physical processes that
 279 result in the production/destruction of H⁻. To investigate whether these behaviors are
 280 present within our H⁻ observations, we start by examining the average flux profiles of
 281 H⁺ and H⁻ using all available orbital data.

282 Figure 5 summarizes the average behavior of precipitating H⁺ and H⁻ fluxes as
 283 a function of CO₂ column density. We see in Panel A that H⁺ fluxes increase steadily
 284 until $\sim 6 \times 10^{14}$ cm⁻², at which point they seemingly plateau. At 5.25×10^{15} cm⁻², we note
 285 a slight increase in the flux relative to this plateau and also see a dramatic falloff in the
 286 flux profile thereafter, decreasing by a factor of ~ 4 . We do not observe such stark be-
 287 havior in Panel B. The H⁻ fluxes do not increase as rapidly with respect to column den-
 288 sity as H⁺. We note, however, that the H⁻ fluxes begin to plateau at $\sim 3 \times 10^{14}$ cm⁻² and
 289 experience a smooth decline starting at 10^{16} cm⁻².

290 We see from Panels A and B that H⁺ is much more favorably created through charge
 291 exchange than H⁻, as indicated by nearly an order of magnitude difference in the av-
 292 erage peak fluxes. This is reflected in Panel C, where we observe a peak flux ratio of ~ 8 .
 293 Across the entire range of column densities, H⁺ flux is ~ 4.5 times greater than that of
 294 H⁻. Clearly, ENAs are preferentially converted to H⁺ along their path of propagation;

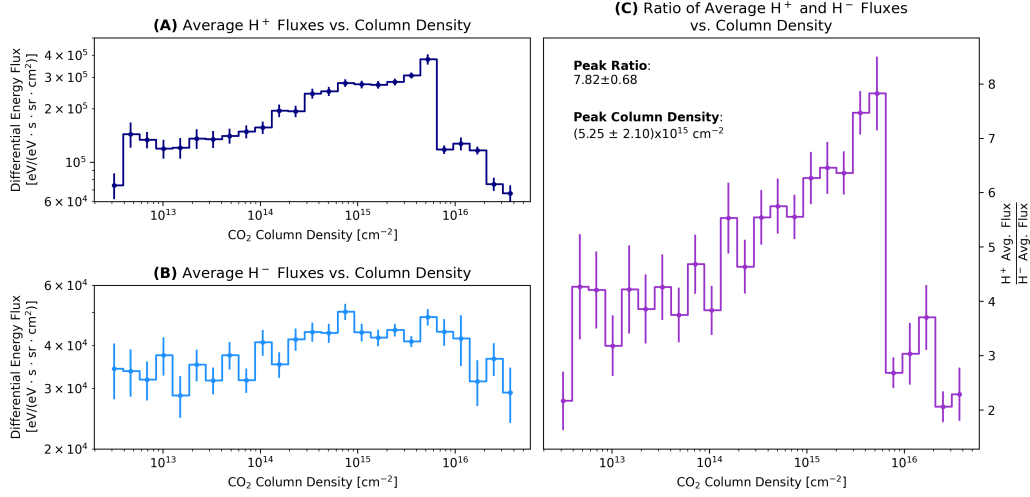


Figure 5. Average profiles of H^+ and H^- fluxes from 43 periapses. (A) Behavior of H^+ flux as a function of CO_2 column density. Mean is taken per column density bin, with the standard error of the mean shown as error bars. (B) Same as Panel A, but for H^- . Note different scaling. (C) Ratio of average H^+ and H^- fluxes versus CO_2 column density.

295 this is not surprising, given the magnitude of the cross sections for electron stripping ver-
 296 sus electron attachment (Lindsay et al., 2005).

297 3 H^- Mathematical Model

298 Previously, Halekas (2017) constructed a simple model for charge equilibrium be-
 299 tween H and H^+ by implementing cross sections for interactions between these two par-
 300 ticle species and CO_2 . They described the evolution of the charged (F^+) and neutral (F^0)
 301 fractions of these populations, respectively, as a function of altitude using a coupled set
 302 of differential equations. Utilizing the same framework, we can repeat this analysis for
 303 H^- .

304 When discussing the behavior of H^- in the atmosphere of Mars, we must consider
 305 three primary processes: electron attachment ($H + CO_2 \rightarrow H^- + CO_2^+$), charge exchange
 306 ($H^- + CO_2 \rightarrow H + CO_2^-$), and photodetachment ($H^- + \gamma \rightarrow H + e^-$). To most accu-
 307 rately represent the behavior of precipitating ENAs, one should compute a weighted sum
 308 over all of the various particle species that these hydrogen ENAs collide with in the up-
 309 per atmosphere. However, for altitudes below 250 km, CO_2 comprises over $\sim 95\%$ of the
 310 Martian atmosphere; thus, it is a reasonable first-order approximation that CO_2 is the
 311 dominant species with which ENAs and their charged byproducts can interact (Nier &
 312 McElroy, 1977; P. R. Mahaffy et al., 2015).

313 Following the framework of Halekas (2017), we can construct a coupled set of equa-
 314 tions describing the evolution of ENAs and H^- as we progress through the Martian at-
 315 mosphere. Accounting for charge exchange, electron attachment, and photodetachment,
 316 we arrive at the following,

$$317 \frac{dF^-}{dr} = [\sigma_{02}(E)F^0(r) - \sigma_{20}(E)F^-(r)]n_{CO_2}(r) - N_{PD}(r, E)F^-(r) \quad (2)$$

$$318 \frac{dF^0}{dr} = [\sigma_{20}(E)F^-(r) - \sigma_{02}(E)F^0(r)]n_{CO_2}(r) + N_{PD}(r, E)F^-(r), \quad (3)$$

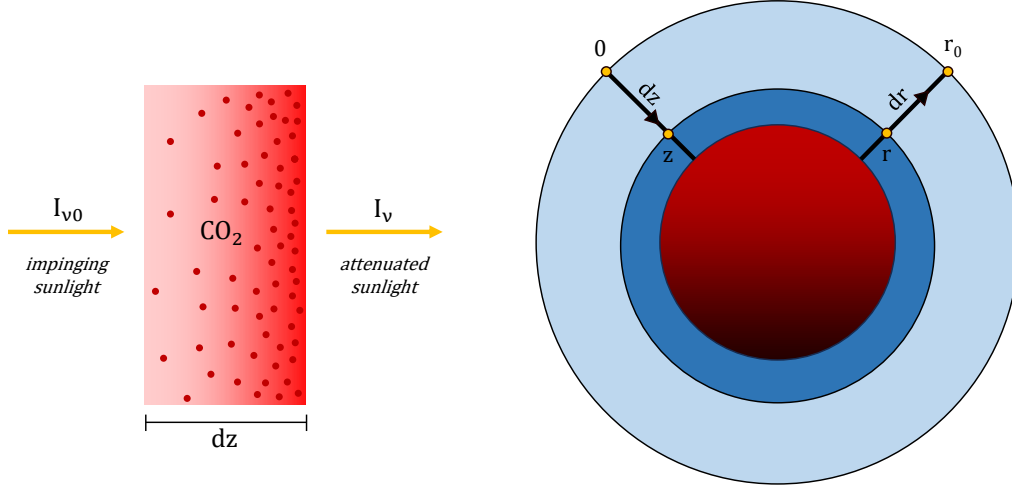


Figure 6. Outline of set up for photodetachment calculation. Left figure shows sunlight ($I_{\nu 0}$) hitting CO_2 slab. Attenuated light (I_{ν}) displayed on right side of slab. Right figure outlines the coordinates implemented in this calculation, with Mars at the center in burgundy. Yellow points show location of integration limits.

319 where F^- is the fraction of precipitating hydrogen ENAs converted to H^- , F^0 is the frac-
 320 tion of H^- converted to ENAs, n_{CO_2} is the CO_2 number density, r is altitude, σ_{02} is the
 321 cross section for electron attachment of H by CO_2 , σ_{20} is the cross section for charge ex-
 322 change of H^- with CO_2 , and N_{PD} represents the number of photodetachments over a
 323 unit distance. We do not include the effects of H^+ charge exchange with CO_2 in this sys-
 324 tem, which can alter F^0 by 4 - 15% (Halekas, 2017); this is left for future examination.
 325 The charge exchange and electron attachment terms within Equations 2 and 3 are well
 326 characterized; however, we need to derive the photodetachment term, N_{PD} .

327 3.1 Photodetachment Term Derivation

328 To determine the number of interactions an impinging particle experiences over a
 329 given time, we can write the following expression,

$$330 \quad k = n\sigma v, \quad (4)$$

331 where n is the number density of the target particle species, σ is the cross section of the
 332 given interaction, and v is the velocity of the impinging particle. This can be easily rewrit-
 333 ten as an interaction rate per unit length if we simply divide Equation 4 by the incom-
 334 ing particle's velocity, v . Examining the first two terms on the right-hand side of Equa-
 335 tions 2 and 3, we can see that the units of these terms are congruent with k/v . There-
 336 fore, we can determine the rate of photodetachment and divide this by the velocity of
 337 H^- in order to determine the number of photodetachments that occur over a given unit
 338 length (N_{PD}).

339 To do this, we first need to determine how solar light is attenuated by the CO_2 domi-
 340 nated Martian atmosphere. This will help us to characterize the rate of photodetach-
 341 ment as a function of altitude as CO_2 density varies. Assuming we have sunlight imping-
 342 ing on a slab of CO_2 , we can write a basic set of equations describing how the flux of sol-
 343 ar photons varies with respect to the thickness of the CO_2 slab (or rather, altitude). Fig-
 344 ure 6 outlines the set up of this problem.

345 From basic radiative processes, we can write the following,

$$346 \quad \frac{dI_\nu(\nu, z)}{dz} = -n_{CO_2}(z)\sigma(\nu)I_\nu(\nu, z), \quad (5)$$

347 where I_ν is the specific intensity of light, dz is the thickness of the CO_2 slab, n_{CO_2} is the
 348 number density, ν is the frequency of light, and σ is the cross section of a given inter-
 349 action between the incoming photons and CO_2 . In principle, the cross section term should
 350 encompass all possible chemical processes, including collisional excitation, absorption,
 351 and emission. However, we only include photoabsorption (σ_{PA}) by CO_2 to simplify our
 352 model.

353 Integrating Equation 5 using the limits described in Figure 6, we arrive at the fol-
 354 lowing,

$$355 \quad \int \frac{dI_\nu(\nu, r)}{I_\nu(\nu, r)} = - \int_r^{r_0} \sigma_{PA}(\nu)n_{CO_2}(r') dr'. \quad (6)$$

356 We can define an expression for atmospheric column density,

$$357 \quad N_{COL} \equiv \int_r^{r_0} n_{CO_2}(r') dr'. \quad (7)$$

358 Utilizing this definition, the integral on the right-hand side of Equation 6 can simply be
 359 expressed as a function of column density,

$$360 \quad \int \frac{dI_\nu(\nu, r)}{I_\nu(\nu, r)} = -\sigma_{PA}(\nu)N_{COL}. \quad (8)$$

361 Evaluating Equation 8 leads to a solution for I_ν ,

$$362 \quad I_\nu(\nu, N_{COL}) = I_{\nu 0}(\nu)e^{-\sigma_{PA}(\nu)N_{COL}}, \quad (9)$$

363 where $I_{\nu 0}(\nu)$ is the solar specific intensity at the top of the Martian atmosphere. Solar
 364 specific intensity is conserved as a function of distance and is well described by the Planck
 365 function for a blackbody emitting at $T = 5,800$ K. Naturally, the solar spectrum is not
 366 a perfect blackbody, as has been shown by previous studies (Huebner et al., 1992; Hueb-
 367 ner & Mukherjee, 2015). However, we utilize this assumption in our calculation to sim-
 368 plify our mathematical model. With all of these moving parts and substituting for en-
 369 ergy, we can finally write I_E as a function of photon energy, blackbody temperature, and
 370 column density,

$$371 \quad I_E(E, T, N_{COL}) = \left(\frac{2E^3}{c^2h^2} \frac{1}{e^{E/kT} - 1} \right) e^{-\sigma_{PA}(E)N_{COL}}. \quad (10)$$

372 As previously mentioned, we seek to quantify the photodetachment rate at a given
 373 point within the Martian atmosphere in order to characterize the fraction of H^- converted
 374 to H due to photodetachment. Now that we have determined how solar radiation is at-
 375 tenuated by CO_2 , we can proceed to calculate the photodetachment rate.

376 The photodetachment rate can be written in the following way,

$$377 \quad k = \int_{\Omega_0}^{\Omega_f} d\Omega \int_{E_0}^{\infty} \frac{I_E(E, T, N_{COL})}{E \cdot h} \sigma_{PD}(E) dE, \quad (11)$$

378 where Ω is the solid angle, and σ_{PD} is the photodetachment cross section (McLaughlin
 379 et al., 2017). Substituting Equation 10 into 11, we arrive at the following,

$$380 \quad k = \int_{\Omega_0}^{\Omega_f} d\Omega \int_{E_0}^{\infty} \sigma_{PD}(E) \left(\frac{2E^2}{c^2h^3} \frac{1}{e^{E/kT} - 1} \right) e^{-\sigma_{PA}(E)N_{COL}} dE. \quad (12)$$

Using simple geometry, we can write the total solid angle through which the solar radiation passes,

$$\Omega = 4\theta \cos(\pi/2 - \theta), \quad (13)$$

where $\theta = \arctan(R_{\odot}/d_{MS})$, R_{\odot} is the radius of the Sun, and d_{MS} is Mars-Sun distance. If we evaluate Equation 13 using Mars-Sun distances for aphelion and perihelion, we obtain $\Omega = [3.1112 \cdot 10^{-5}, 4.5221 \cdot 10^{-5}]$ steradians, respectively.

Combining Equations 12 and 13, we arrive at our final solution describing the rate of photodetachment at a given CO_2 column density in the Martian atmosphere,

$$k = 4\theta \cos(\pi/2 - \theta) \int_{E_0}^{\infty} \sigma_{PD}(E) \left(\frac{2E^2}{c^2 h^3} \frac{1}{e^{E/kT} - 1} \right) e^{-\sigma_{PA}(E)N_{COL}} dE. \quad (14)$$

We can see from Equation 14 that there are still two undefined parameters: $\sigma_{PD}(E)$ and $\sigma_{PA}(E)$. These variables quantify photodetachment and photoabsorption cross sections, respectively, and do not have analytical forms. We therefore implement measured values of these parameters across various photon energies to obtain a numerical solution for k (Chandrasekhar, 1945; Branscomb & Smith, 1955; Sun & Weissler, 1955; Smith & Burch, 1959; Cairns & Samson, 1965; Conrath et al., 1973; Wishart, 1979; Craver, 1982; Lewis & Carver, 1983; Rahman & Hird, 1986; Yoshino et al., 1996; Parkinson et al., 2003; Stark et al., 2007; McLaughlin et al., 2017).

One aspect to note is the temperature dependence of the photoabsorption cross sections utilized in this study. As we progress through the Martian atmosphere, the temperature profile varies. In the case of CO_2 in the range of altitudes we examine, the temperature varies from approximately 180 K to 245 K (Stone et al., 2018). The photoabsorption cross sections utilized in our calculations were obtained at a temperature of 195 K; thus, our photodetachment rate will be an approximation based on the assumption that CO_2 photoabsorption cross sections do not vary significantly with temperature.

We can determine k by implementing the various measured cross sections for photodetachment and photoabsorption. To do so, we integrate Equation 12 over energies where photodetachment cross sections are nonzero. From Supplemental Figure S1, we see that the relevant energy ranges fall between the near infrared and EUV. Previous measurements have demonstrated that Martian atmospheric transmittance of solar photons is most impeded by CO_2 in the infrared at wavelengths between ~ 2 and $13 \mu\text{m}$ (Conrath et al., 1973). If we examine Supplemental Figure S1, we find that these near infrared wavelengths are outside the domain where photodetachment is prevalent. The infrared photoabsorption cross sections are therefore irrelevant, since the photodetachment cross section tends towards zero in this frequency range. We do note, however, that there is an overlap in photoabsorption and photodetachment in the EUV regime and proceed to evaluate Equation 14 over this frequency range.

Integrating Equation 14 over energies $\sim 10^{-1} - 10^5$ eV, we obtain a photodetachment rate that depends only on Mars-Sun distance. Upon evaluating Equation 14 for column densities $10^9 - 10^{18} \text{ cm}^{-2}$ for a given Mars-Sun distance, we observe a $(9.25 \times 10^{-6})\%$ change in the photodetachment rate between the maximum and minimum column density. This indicates that attenuation due to CO_2 photoabsorption is negligible, and thus the column density dependence in Equation 14 can be neglected.

With these results, we can further simplify Equation 14. If we set the photoabsorption term ($e^{-\sigma_{PA}(E)N_{COL}}$) to unity and integrate over all EUV energies, our integrand simplifies to $2.0244 \times 10^5 \text{ s}^{-1} \text{ sr}^{-1}$. We can now express the rate of photodetachment in the following manner,

$$k = (2.0244 \times 10^5) [4\theta \cos(\pi/2 - \theta)]. \quad (15)$$

Evaluating the above equation during aphelion and perihelion results in photodetachment rates of ~ 6 and ~ 9 per second, respectively. This is in relatively good agree-

430 ment with photodetachment rates obtained in previous studies using measured solar pho-
 431 ton flux at 1 AU (Huebner et al., 1992; Desai et al., 2021). Extrapolating the results from
 432 these studies to Mars (i.e., 1.3814 - 1.666 AU) results in rates between ~ 5 and ~ 7 pho-
 433 todetachments per second, which is congruent with our derivation.

434 If we recall Equation 4, we can now write $N_{PD} = k/v_{H^-} = k\sqrt{m_{H^-}/2E}$, where
 435 m_{H^-} is the mass of H^- . This allows us to write a full expression describing the behav-
 436 ior of hydrogen ENAs and H^- as they interact with both solar photons and the Mar-
 437 tian atmosphere:

$$438 \frac{dF^-}{dr} = [\sigma_{02}(E)F^0(r) - \sigma_{20}(E)F^-(r)]n_{CO_2}(r) - (2.0244 \times 10^5) [4\theta \cos(\pi/2 - \theta)] \sqrt{\frac{m_{H^-}}{2E}} F^-(r) \quad (16)$$

$$439 \frac{dF^0}{dr} = [\sigma_{20}(E)F^-(r) - \sigma_{02}(E)F^0(r)]n_{CO_2}(r) + (2.0244 \times 10^5) [4\theta \cos(\pi/2 - \theta)] \sqrt{\frac{m_{H^-}}{2E}} F^-(r). \quad (17)$$

440 3.2 Numerical and Analytical Solutions

441 Before explicitly solving Equations 16 and 17, we can examine how the number of
 442 interactions per unit length for electron attachment, charge exchange, and photodetach-
 443 ment varies with respect to CO_2 atmospheric density by quantifying each coefficient within
 444 these coupled differential equations. Utilizing the cross sections for electron attachment
 445 and charge exchange collected between 1 and 3 keV, we can calculate the quantity of each
 446 coefficient within Equations 16 and 17 and determine at which point within the Mar-
 447 tian atmosphere a given process dominates (Nakai et al., 1987; Lindsay et al., 2005). Fig-
 448 ure 7 summarizes how these three processes vary with respect to altitude using this ap-
 449 proach.

450 It is important to note that the cross section for charge exchange between H^- and
 451 CO_2 has not been measured within the energy range we examine here. Previous stud-
 452 ies have utilized O_2 cross sections to generate proxy cross sections for CO_2 when mea-
 453 surements were not available (Kallio & Barabash, 2000, 2001). We employ this method
 454 in our analysis as well.

455 Nakai et al. (1987) measured the cross section of charge exchange between H^- and
 456 O_2 for energies spanning 1 eV to 10 MeV. They also measured the cross section of charge
 457 exchange between H^- and CO_2 (σ_{20} in our analysis), but only at energies greater than
 458 20 keV. In order to extrapolate σ_{20} to solar wind energies, we employ a scaling factor.
 459 We average the ratio of the O_2 cross section to the CO_2 cross section in the 20 keV to
 460 10 MeV range. We then multiply the entire O_2 cross section profile by this average ra-
 461 tio to obtain proxy values of σ_{20} at energies pertinent for our analysis here (Nakai et al.,
 462 1987).

463 We observe a few interesting behaviors in Figure 7. First and foremost, we see in
 464 Panels A and B that charge exchange is the primary process governing H^- for altitudes
 465 below 194 ± 5 km across various energies and Mars-Sun distances. Above this thresh-
 466 old, however, we note that photodetachment overtakes both electron attachment and charge
 467 exchange processes. Further examination of Panel A indicates that the altitude range
 468 at which electron attachment overtakes photodetachment is much lower than that of charge
 469 exchange. Panel B shows that photodetachment remains significantly important com-
 470 pared to electron attachment at altitudes above 134 ± 8 km. This feature becomes most
 471 important at perihelion for low energy solar wind conditions. Figure 7 indicates that pho-
 472 todetachment becomes relatively negligible at ionospheric altitudes below ~ 125 km. How-
 473 ever, in the upper ionosphere, it appears that this H^- sink cannot be ignored.

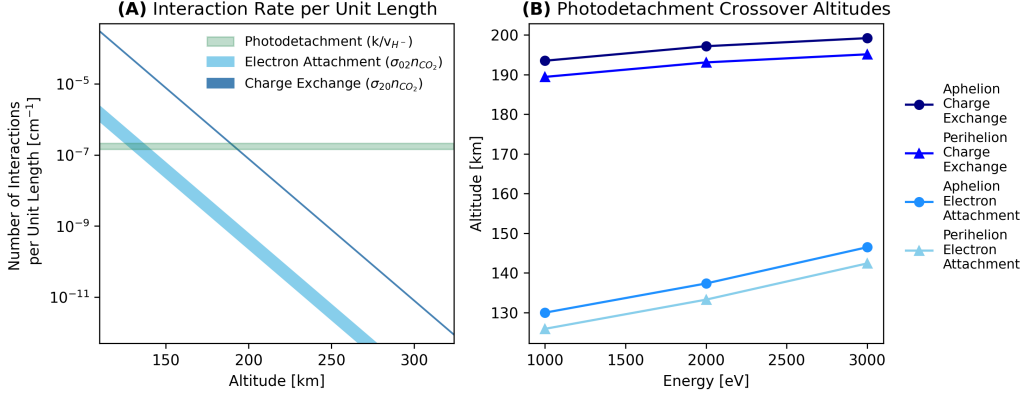


Figure 7. Summary of interactions per unit length for charge exchange, electron attachment, and photodetachment. (A) The upper bound for electron attachment was determined using cross sections at 3 keV, while the lower bound was determined using 1 keV cross sections. The inverse of this applies to the charge exchange curve. The upper bound of the photodetachment curve represents the value at perihelion for $E_{H^-} = 1$ keV, while the lower bound is at aphelion. The altitude values and corresponding density values were calculated using the average CO₂ profile from Supplemental Figure S2. (B) Summary of altitudes at which photodetachment becomes dominated by either charge exchange or electron attachment (i.e., where the blue regions overlap the green region in Panel A). Curves are separated by Mars-Sun distance and relevant process, as indicated in legend.

3.2.1 Analytical Solution Derivation

For altitudes below 125 km, we can find an approximate solution to Equations 16 and 17 by assuming $k \rightarrow 0$. This leaves us with differential equations in the following form,

$$\frac{dF^-}{dr} = [\sigma_{02}F^0(r) - \sigma_{20}F^-(r)]n_{CO_2}(r) \quad (18)$$

$$\frac{dF^0}{dr} = [\sigma_{10}F^-(r) - \sigma_{01}F^0(r)]n_{CO_2}(r). \quad (19)$$

If we add Equations 18 and 19, we find that $\frac{dF^-}{dr} = -\frac{dF^0}{dr}$. This, combined with the boundary conditions of $F^-(\infty) = 0$ and $F^0(\infty) = 1$, results in

$$F^0(r) = 1 - F^-(r). \quad (20)$$

We can write the density in Equations 18 and 19 analytically if we assume that the atmosphere is in equilibrium. This is true for altitudes below 300 km in the Martian atmosphere, which is approximately the upper limit of the altitudes we examine here (Cravens et al., 2017). We can write the CO₂ density profile in an exponential form,

$$n_{CO_2}(r) = N_0 e^{mr}, \quad (21)$$

where N_0 is a reference CO₂ number density, and the magnitude of m is the inverse of the atmospheric scale height. Substituting Equations 20 and 21 into Equation 18, we are left with a differential equation in the following form:

$$\frac{dF^-}{dr} + (\sigma_{02} + \sigma_{20})N_0 e^{mr} - \sigma_{02}N_0 e^{mr} = 0. \quad (22)$$

492 Equation 22 has a solution for the negative charge fraction,

$$493 \quad F^-(r) = \frac{\sigma_{02}}{\sigma_{02} + \sigma_{20}} \left[1 - e^{-\frac{N_0(\sigma_{02} + \sigma_{20})}{m} e^{mr}} \right]. \quad (23)$$

494 Recalling Equation 7, we can rewrite the argument of the exponent in Equation
495 23 as a function of CO₂ column density. Substituting Equation 7 into Equation 23 and
496 utilizing Equation 20 to solve for F⁰(r), we arrive at approximate analytic solutions for
497 the negative and neutral fractions,

$$498 \quad F^-(r) = \frac{\sigma_{02}}{\sigma_{02} + \sigma_{20}} \left[1 - e^{-(\sigma_{02} + \sigma_{20})N_{COL}} \right] \quad (24)$$

$$499 \quad F^0(r) = \frac{\sigma_{20}}{\sigma_{02} + \sigma_{20}} \left[1 + \frac{\sigma_{02}}{\sigma_{20}} e^{-(\sigma_{02} + \sigma_{20})N_{COL}} \right]. \quad (25)$$

500 If we assume that precipitating solar wind hydrogen atoms reach approximate equi-
501 librium after one e-folding scale, we can determine from Equations 24 and 25 the equi-
502 librium charge fraction, neutral fraction, and column density. Utilizing this assumption,
503 we arrive at an equilibrium column density,

$$504 \quad CD_{eq} = \frac{1}{\sigma_{02} + \sigma_{20}}. \quad (26)$$

505 The negative and neutral fractions converge over ~5 e-folding scales to a final value
506 expressed by the following equations,

$$507 \quad F_f^- \simeq \frac{\sigma_{02}}{\sigma_{02} + \sigma_{20}} \quad (27)$$

$$508 \quad F_f^0 \simeq \frac{\sigma_{20}}{\sigma_{02} + \sigma_{20}}. \quad (28)$$

509 The electron stripping and charge exchange cross sections vary with respect to the
510 energy of the incoming particle; thus, depending on upstream solar wind conditions, we
511 would anticipate precipitating solar wind hydrogen to reach equilibrium at different col-
512 umn densities within the Martian atmosphere. Using NGIMS CO₂ data, we can explic-
513 itly obtain the fit parameters in Equation 21 that describe the average CO₂ density pro-
514 file as a function of altitude to accurately evaluate Equations 24 and 25. The results of
515 this fitting procedure on inbound verified CO₂ data can be seen in Supplemental Fig-
516 ure S2. These fit parameters, N_0 and m , are then implemented in our column density
517 calculation.

518 **3.2.2 Analytical and Numerical Solution Comparison**

519 As we progress through the atmosphere, we expect the solutions to Equations 16
520 and 17 to converge to Equations 24 and 25, respectively. However, to understand the role
521 that photodetachment plays at altitudes above 125 km, we can find precise solutions to
522 Equations 16 and 17 across various solar wind energies and Mars-Sun distances using
523 numerical integration methods¹

524 Examining the numerical solution for F⁻ in Figure 8, we find that the maximum
525 charge fraction is 0.78% for high energy solar wind conditions. For lower energy solar
526 wind conditions, this decreases to 0.29%. Kallio et al. (1997) demonstrated that 1-3%

¹ These equations were solved using NDSolve in Mathematica with altitude bounds of 100 - 500 km. The boundary conditions were approximated at an altitude of 500 km. The values of N_0 and m implemented in these calculations can be found in Supplemental Figure S2.

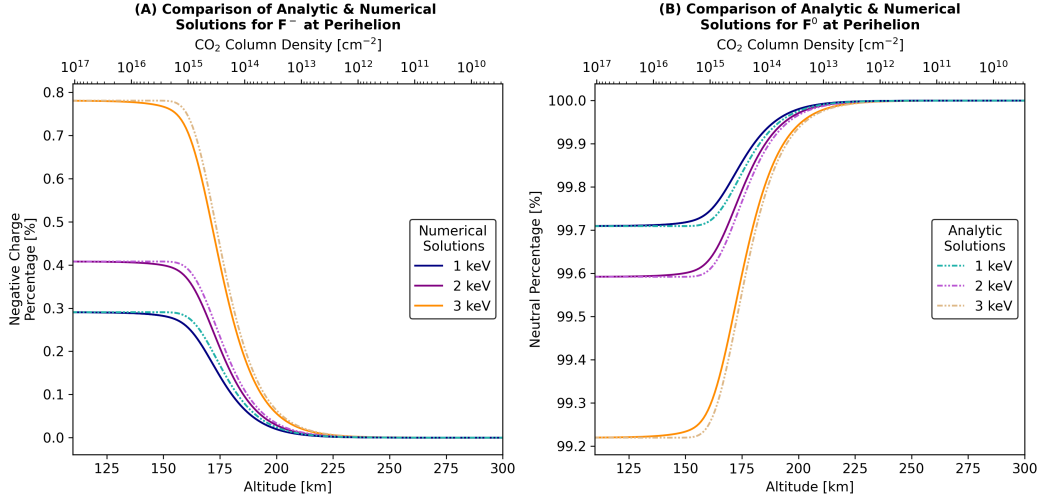


Figure 8. Summary of numerical and analytical solutions for F^- and F^0 at perihelion. Numerical solutions (solid) are obtained from Equations 16 and 17. Analytic solutions (dashed-dotted) are obtained from Equations 24 and 25.

527 of solar wind protons are converted to ENAs for the energy range we examine here. Com-
 528 bining this with the observed charge fractions determined from our model, this implies
 529 that we would anticipate observing 0.0029 - 0.023% of the upstream solar wind proton
 530 flux in the form of H^- ions.

531 Figure 8 summarizes the numerical and analytical solutions across various solar wind
 532 energies at perihelion for F^- and F^0 . We only examine the results at perihelion since the
 533 numerical model does not change significantly as a function of Mars-Sun distance (see
 534 Supplemental Figure S3). We see in both panels that there is a slight divergence between
 535 the numerical and analytical solutions at altitudes between 130 and 200 km. We find that
 536 the fraction of ENAs converted to H^- is slightly lower in the numerical model compared
 537 to the analytical model, suggesting that photodetachment is playing a role in depleting
 538 the H^- population. If we examine these plots more carefully, we find that the maximum
 539 percent difference between the numerical and analytical charge fractions is 1 - 7%. For
 540 typical solar wind fluxes ($\sim 10^8 \text{ cm}^{-2} \text{ s}^{-1}$), we would anticipate a flux of H^- on the order
 541 of $\sim 10^3 - 10^4 \text{ cm}^{-2} \text{ s}^{-1}$. In order to detect the effects of photodetachment, we would
 542 need to be able to measure fluctuations of $\sim 10 - 10^3 \text{ cm}^{-2} \text{ s}^{-1}$. With SWEA's sensitiv-
 543 ity, we would not be able to observe these differences; higher flux H^- events would be
 544 required to detect any deviations.

545 In general, H^- is not preferentially generated in the Martian environment due to
 546 the fact that it is so energetically unfavorable. We find that photodetachment dominates
 547 the $H-H^-$ system in the upper ionosphere, while atmospheric collisional processes pri-
 548 marily govern these particles below 200 km. We observe a slight difference between our
 549 modeling results when photodetachment is included versus when it is excluded. We see
 550 a minute increase in the ENAs generated from this process. In practice, this difference
 551 would be extremely difficult to observe given our current instrumentation. Only during
 552 high energy solar wind conditions would we potentially be able to see the changes in the
 553 negative charge fraction induced by photodetachment.

4 Data-Model Comparison

We can now directly compare our observational results from Section 2 to our modeling results from Section 3. Below we will discuss how various aspects of our mathematical model compare to the MAVEN observations previously discussed.

We find that there is not a clear difference in the observed charge fractions as a function of Mars-Sun distance as shown in Supplemental Figure S3, indicating that H^- should be observed throughout various points within the Martian orbit. Figures 3 and 4 indicate that H^- is, however, preferentially observed near perihelion. This is not necessarily contradictory of our model; we do not incorporate variable conditions within the hydrogen corona or lower atmosphere in our framework. Previous studies have found that there is a clear seasonal (and consequently, Mars-Sun distance) dependence on the observed ENA and H^+ flux due to a factor of 3 increase in the exposed hydrogen column density (Halekas et al., 2015; Halekas, 2017). This expansion of the corona creates a larger deposition of ENAs, increasing the likelihood of conversion to H^+ and H^- within the CO_2 atmosphere. It has also been shown that the Martian atmosphere heats and consequently expands during southern summer, affecting hydrogen deposition and CO_2 densities (Halekas et al., 2015; Halekas, 2017; Hughes et al., 2019). These factors would also affect our numerical solutions, shifting them to higher altitudes at perihelion versus aphelion.

Revisiting the trends presented in Figure 4, we observe H^- precipitation at various points within the solar cycle. In principle, we would expect solar EUV emission to affect our observations due to the influence of photodetachment. However, Figure 8 demonstrates the charge fraction is only slightly influenced by this process at altitudes below 200 km. Figure 8 clearly shows that the primary factor at play is the upstream solar wind energy, which greatly impacts the observed charge fraction. Figure 3 bolsters this fact, showing that H^- events are distributed across various solar conditions but occur most often during high energy solar wind conditions.

Additionally, we can directly compare observed number fluxes of the upstream solar wind with those of downstream H^- to determine if the limiting charge fractions that we found in our model align well with observations. We implement the solar wind proxy data for each of our 43 orbits and determine the number flux using the given parameters. In order to compute the density of H^- and H^+ for a given measurement, we utilize the downward, background-corrected differential energy fluxes that we compute in Section 2.1. We then implement Equation 29 for each available measurement,

$$n = \sqrt{\frac{m}{2}} \Delta\Omega \sum_{i=1}^n E_i^{-3/2} \Delta E_i F(E_i), \quad (29)$$

where m is the mass of hydrogen, $\Delta\Omega$ is the solid angle, ΔE is the energy channel resolution, E is the energy, $F(E)$ is the differential energy flux, and i is the index of a given energy channel. For the SWEA data, we compute this sum for energies above 800 eV to best isolate H^- from other high flux populations (Jones et al., 2022). We repeat this computation for SWIA for energies spanning 300 to 4,000 eV in order to exclude spacecraft charging signatures in addition to pickup ions. Figure 9 summarizes our findings.

Recalling from Section 3.2.2, we anticipate 0.04 - 0.45% of upstream solar wind protons to be converted to H^+ (Halekas, 2017) and 0.0029 - 0.0234% to H^- . Panels B and C summarize the observed conversion efficiency for these populations, respectively. We see in Panel B that the conversion rate from solar wind protons to downstream H^+ is $\sim 0.8\%$ across all energies, which is higher than the aforementioned anticipated limits. However, if we increase these limits by a factor of 3 to account for expansion of the hydrogen corona at perihelion (hashed region in Figure 9B), we find that the observed conversion rate aligns well with the model outlined in Halekas (2017). If we now look at the corresponding results in Panel C for H^- , we observe a $\sim 0.1\%$ conversion rate, which is much higher than our derived limits. We do observe slight overlap between the lower limit

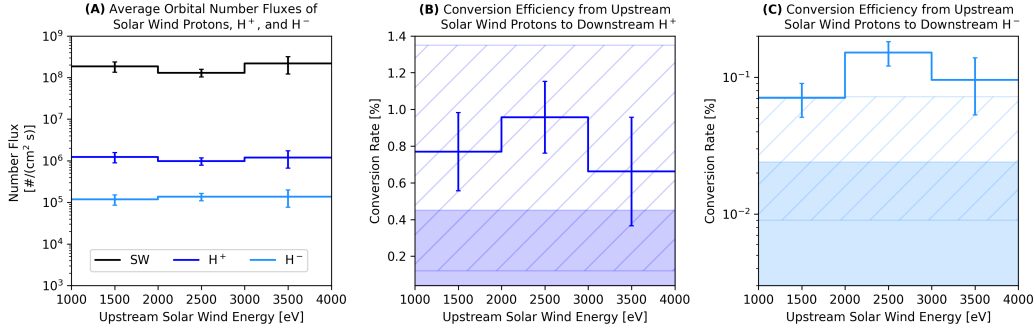


Figure 9. Summary of solar wind, H⁺, and H⁻ orbital fluxes and corresponding conversion rates. (A) Orbit-averaged number fluxes for upstream solar wind protons (black), downstream H⁺ (blue), and downstream H⁻ (light blue). Errorbars correspond to the standard error of the mean for a given bin. (B) Percent of solar wind protons converted to H⁺. (C) Percent of solar wind protons converted to H⁻. Shaded regions in B and C represent the percentage ranges based on our computations in Section 3.2.2 and previous findings (Kallio et al., 1997; Halekas, 2017). Hashed regions represent anticipated percentages at perihelion.

604 of our observations and the upper limit of the conversion rate at perihelion. This dis-
 605 crepancy between our model and observations may stem from an overestimation of σ_{20} .
 606 Smaller values of σ_{20} would result in larger values of F^- across all solar wind energies.
 607 Further investigation is required to better understand this behavior, and direct measure-
 608 ments of σ_{20} at solar wind energies would be extremely beneficial.

609 Examining Equation 26, we find that the turnover column densities for H⁻ and H⁺
 610 span $(3.068 \pm 0.059) \times 10^{14} \text{ cm}^{-2}$ and $(6.426 \pm 0.140) \times 10^{14} \text{ cm}^{-2}$ for energies falling be-
 611 tween 1 and 3 keV, respectively (Nakai et al., 1987; Lindsay et al., 2005; Halekas, 2017).
 612 Comparing these values to the observed trends in Figure 5, we see that the observed pro-
 613 files for both particle populations begin to plateau at these aforementioned column den-
 614 sity values. This indicates that H⁺ and H⁻ do approximately equilibrate after one e-folding
 615 scale, as was estimated by Equation 26.

616 We can also compare the observed abundance of H⁺ with respect to H⁻ to what
 617 we would expect given the conversion rate of ENAs to each particle species. In Figure
 618 5, we note that the peak ratio of H⁺ to H⁻ fluxes in Panel C is ~ 8 . From our analysis
 619 in Section 3.2.2, we can determine the anticipated ratio of H⁺ flux to H⁻ flux. We pre-
 620 dicted that 0.29 - 0.78% of ENAs are converted to H⁻, while Halekas (2017) determined
 621 that 4 - 15% of ENAs are converted to H⁺. Using these limits, we can anticipate H⁺ to
 622 be ~ 13 - 19 times more abundant than H⁻. These values are ~ 2 times higher than the
 623 maximum observed ratio in Figure 5. This discrepancy is not surprising, given the con-
 624 version rates obtained in Figure 9. From our observations, we would anticipate a H⁺/H⁻
 625 ratio of ~ 10 , which is more in line with what we observe in Figure 5.

626 5 Summary

627 Using MAVEN data, we determine under what conditions H⁻ is best observed and
 628 compare fluxes of H⁻ and H⁺ as a function of CO₂ column density. Using various meth-
 629 ods, we isolate orbits with H⁻ signatures and determine that precipitation of this par-
 630 ticle population is incredibly rare (1.8% of available observations). We also find that these
 631 particles are best observed during periods of high energy solar wind near perihelion; more
 632 of these events may become observable by MAVEN as we approach solar maximum, dur-

ing which high energy solar events (i.e., CIRs, SIRs, CMEs) become more frequent. We observe no clear correlation between solar EUV irradiance or solar cycle with H^- observations. Lastly, we find that H^+ is preferentially generated from precipitating solar wind hydrogen ENAs compared to H^- . On average, H^+ fluxes are 4.5 times greater than observed H^- fluxes as a function of CO_2 column density.

We develop a simple model describing the equilibrium conditions for H^- in the Martian atmosphere by building off of a framework previously constructed by Halekas (2017). We consider the effects of charge exchange, electron attachment, and photodetachment in our model. We find numerical solutions for the charge (F^-) and neutral fractions (F^0) and determine the converging charge fraction to span 0.29 - 0.78% depending on upstream solar wind energy. We do not observe a significant change in the numerical solutions for F^- or F^0 between perihelion and aphelion. We find that the maximum difference between the analytical and numerical solutions when photodetachment is incorporated is 1 - 7%, occurring between 125 and 250 km.

When comparing our model to observations, we find good agreement in the equilibrium column densities for H^- and H^+ . We observe a slight discrepancy in the observed charge fraction of H^- compared to our model, which underestimates our observations. We also find that the ratio of observed H^+/H^- fluxes is smaller than anticipated with our given model parameters. Further observations of H^- are needed to better understand the discrepancies discussed here.

Future work could compare the conditions under which we observe H^- , H^+ , and proton aurora at Mars. Determining the distribution of these events will help us to better understand the Mars-solar wind interaction, as well as the primary factors governing the precipitation of hydrogen ENAs. The model describing H^- precipitation could also be expanded upon, accounting for hydrogen depletion caused by H^+ charge exchange with CO_2 , seasonal variability of the hydrogen corona, as well as solar zenith angle dependencies. These two latter parameters greatly affect observed hydrogen deposition at Mars and are worth investigating (Halekas, 2017; Henderson et al., 2021; Hughes et al., 2019, 2023). It would also be of great scientific value to obtain direct measurements of electron stripping of H^- by CO_2 at solar wind energies to better constrain these processes as well.

6 Open Research

All MAVEN data utilized in this project are available on the NASA Planetary Data System. MAVEN SWIA data can be found here: <https://pds-ppi.igpp.ucla.edu/mission/MAVEN/MAVEN/SWIA>. MAVEN NGIMS data are available here: <https://pds-ppi.igpp.ucla.edu/mission/MAVEN/MAVEN/NGIMS>. MAVEN EUVM data are located here: <https://pds-ppi.igpp.ucla.edu/mission/MAVEN/MAVEN/EUV>. MAVEN SWEA data can be found at the following link: <https://pds-ppi.igpp.ucla.edu/mission/MAVEN/MAVEN/SWEA>. Photodetachment cross section data were curated by McLaughlin et al. (2017). Photoabsorption cross sections were obtained from multiple sources and can be found compiled at Henderson et al. (2023). Electron attachment cross sections can be found in Lindsay et al. (2005), and H^- charge exchange cross sections obtained in Section 3.2 can be found at Henderson et al. (2023). Solar wind data can also be found at Henderson et al. (2023).

Acknowledgments

The authors would like to acknowledge the MAVEN contract for support. We would also like to thank Dr. Casey DeRoo and Dr. Steve Spangler for their insightful conversations throughout this project.

References

- 681
682 Anderson Jr., D. E. (1974). Mariner 6, 7, and 9 Ultraviolet Spectrometer Ex-
683 periment: Analysis of hydrogen Lyman alpha data. *Journal of Geophysical*
684 *Research (1896-1977)*, 79(10), 1513-1518. doi: [https://doi.org/10.1029/
685 JA079i010p01513](https://doi.org/10.1029/JA079i010p01513)
- 686 Bisikalo, D. V., Shematovich, V. I., Gérard, J.-C., & Hubert, B. (2018). Monte
687 Carlo Simulations of the Interaction of Fast Proton and Hydrogen Atoms
688 with the Martian Atmosphere and Comparison With In Situ Measurements.
689 *Journal of Geophysical Research: Space Physics*, 123(7), 5850-5861. doi:
690 <https://doi.org/10.1029/2018JA025400>
- 691 Branscomb, L. M., & Smith, S. J. (1955, May). Experimental cross section for pho-
692 todetachment of electrons from h^- and d^- . *Phys. Rev.*, 98, 1028–1034. doi: 10
693 .1103/PhysRev.98.1028
- 694 Brecht, S. H. (1997). Solar wind proton deposition into the Martian atmosphere.
695 *Journal of Geophysical Research: Space Physics*, 102(A6), 11287-11294. doi:
696 <https://doi.org/10.1029/97JA00561>
- 697 Brinkfeldt, K., Gunell, H., Brandt, P. C., Barabash, S., Frahm, R., Winningham, J.,
698 ... Dierker, C. (2006). First ENA observations at Mars: Solar-wind ENAs
699 on the nightside. *Icarus*, 182(2), 439-447. (Results from the Mars Express
700 ASPERA-3 Investigation) doi: <https://doi.org/10.1016/j.icarus.2005.12.023>
- 701 Cairns, R. B., & Samson, J. A. R. (1965). Absorption and photoionization cross
702 sections of co_2 , co , ar , and he at intense solar emission lines. *Journal of Geo-*
703 *physical Research (1896-1977)*, 70(1), 99-104. doi: [https://doi.org/10.1029/
704 JZ070i001p000099](https://doi.org/10.1029/JZ070i001p000099)
- 705 Chaffin, M. S., Kass, D. M., Aoki, S., Fedorova, A. A., Deighan, J., Connour,
706 K., ... Korablev, O. I. (2021, October). Martian water loss to space en-
707 hanced by regional dust storms. *Nature Astronomy*, 5, 1036-1042. doi:
708 [10.1038/s41550-021-01425-w](https://doi.org/10.1038/s41550-021-01425-w)
- 709 Chandrasekhar, S. (1945, September). On the Continuous Absorption Coefficient
710 of the Negative Hydrogen Ion. *The Astrophysical Journal*, 102, 223. doi: 10
711 .1086/144755
- 712 Chaufray, J., Bertaux, J., Leblanc, F., & Quémerais, E. (2008). Observation of the
713 hydrogen corona with SPICAM on Mars Express. *Icarus*, 195(2), 598-613. doi:
714 <https://doi.org/10.1016/j.icarus.2008.01.009>
- 715 Conrath, B., Curran, R., Hanel, R., Kunde, V., Maguire, W., Pearl, J., ... Burke,
716 T. (1973). Atmospheric and surface properties of mars obtained by infrared
717 spectroscopy on mariner 9. *Journal of Geophysical Research (1896-1977)*,
718 78(20), 4267-4278. doi: <https://doi.org/10.1029/JB078i020p04267>
- 719 Cravens, T. E., Hamil, O., Houston, S., Bougher, S., Ma, Y., Brain, D., & Ledv-
720 ina, S. (2017). Estimates of ionospheric transport and ion loss at Mars.
721 *Journal of Geophysical Research: Space Physics*, 122, 10626–10637. doi:
722 <https://doi.org/10.1002/2017JA024582>
- 723 Craver, C. D. (1982). *The coblenz society desk book of infrared spectra*. (2nd ed.
724 ed.). Kirkwood, MO: The Society.
- 725 Deighan, J., Jain, S. K., Chaffin, M. S., Fang, X., Halekas, J. S., Clarke, J. T., ...
726 Jakosky, B. M. (2018, July). Discovery of a proton aurora at Mars. *Nature*
727 *Astronomy*, 2, 802-807. doi: [10.1038/s41550-018-0538-5](https://doi.org/10.1038/s41550-018-0538-5)
- 728 Desai, R. T., Zhang, Z., Wu, X., & Lue, C. (2021, may). Photodetachment and test-
729 particle simulation constraints on negative ions in solar system plasmas. *The*
730 *Planetary Science Journal*, 2(3), 99. doi: [10.3847/PSJ/abf638](https://doi.org/10.3847/PSJ/abf638)
- 731 Diéval, C., Kallio, E., Barabash, S., Stenberg, G., Nilsson, H., Futaana, Y., ...
732 Brain, D. A. (2012). A case study of proton precipitation at Mars: Mars Ex-
733 press observations and hybrid simulations. *Journal of Geophysical Research:*
734 *Space Physics*, 117(A6). doi: <https://doi.org/10.1029/2012JA017537>
- 735 Eparvier, F., Chamberlin, P., & Woods, T. (2015). The Solar Extreme Ultraviolet

- 736 Monitor for MAVEN. *Space Sci Rev*, 195, 293–301. doi: <https://doi.org/10>
737 .1007/s11214-015-0195-2
- 738 Futaana, Y., Barabash, S., Grigoriev, A., Holmström, M., Kallio, E., Brandt, P. C.,
739 ... Dierker, C. (2006a). First ENA observations at Mars: ENA emissions
740 from the Martian upper atmosphere. *Icarus*, 182(2), 424-430. (Results from
741 the Mars Express ASPERA-3 Investigation) doi: <https://doi.org/10.1016/j>
742 j.icarus.2005.09.019
- 743 Futaana, Y., Barabash, S., Grigoriev, A., Holmström, M., Kallio, E., Brandt, P. C.,
744 ... Dierker, C. (2006b). First ENA observations at Mars: Subsolar ENA
745 jet. *Icarus*, 182(2), 413-423. (Results from the Mars Express ASPERA-3
746 Investigation) doi: <https://doi.org/10.1016/j>
747 j.icarus.2005.08.024
- 747 Girazian, Z., & Halekas, J. (2021). Precipitating Solar Wind Hydrogen at Mars:
748 Improved Calculations of the Backscatter and Albedo With MAVEN Obser-
749 vations. *Journal of Geophysical Research: Planets*, 126(2), e2020JE006666.
750 (e2020JE006666 2020JE006666) doi: <https://doi.org/10.1029/2020JE006666>
- 751 Gunell, H., Brinkfeldt, K., Holmström, M., Brandt, P. C., Barabash, S., Kallio,
752 E., ... Dierker, C. (2006). First ENA observations at Mars: Charge
753 exchange ENAs produced in the magnetosheath. *Icarus*, 182(2), 431-
754 438. (Results from the Mars Express ASPERA-3 Investigation) doi:
755 <https://doi.org/10.1016/j>
756 j.icarus.2005.10.027
- 756 Halekas, J. S. (2017). Seasonal variability of the hydrogen exosphere of Mars. *Jour-*
757 *nal of Geophysical Research: Planets*, 122(5), 901-911. doi: <https://doi.org/10>
758 .1002/2017JE005306
- 759 Halekas, J. S., Lillis, R. J., Mitchell, D. L., Cravens, T. E., Mazelle, C., Connerney,
760 J. E. P., ... Ruhunusiri, S. (2015). MAVEN observations of solar wind hy-
761 drogen deposition in the atmosphere of Mars. *Geophysical Research Letters*,
762 42(21), 8901-8909. doi: <https://doi.org/10.1002/2015GL064693>
- 763 Halekas, J. S., Ruhunusiri, S., Harada, Y., Collinson, G., Mitchell, D. L., Mazelle,
764 C., ... Jakosky, B. M. (2017). Structure, dynamics, and seasonal variability
765 of the Mars-solar wind interaction: MAVEN Solar Wind Ion Analyzer in-flight
766 performance and science results. *Journal of Geophysical Research: Space*
767 *Physics*, 122(1), 547-578. doi: <https://doi.org/10.1002/2016JA023167>
- 768 Halekas, J. S., Taylor, E. R., Dalton, G., Johnson, G., Curtis, D. W., McFadden,
769 J. P., ... Jakosky, B. M. (2015). The Solar Wind Ion Analyzer for MAVEN.
770 *Space Science Reviews*, 195(1-4), 125-151. doi: 10.1007/s11214-013-0029-z
- 771 Henderson, S., Halekas, J., Girazian, Z., Espley, J., & Elrod, M. (2022). Influence
772 of Magnetic Fields on Precipitating Solar Wind Hydrogen at Mars. *Geophys-*
773 *ical Research Letters*, 49(12), e2022GL099114. (e2022GL099114 2022GL099114)
774 doi: <https://doi.org/10.1029/2022GL099114>
- 775 Henderson, S., Halekas, J., Jolitz, R., Mitchell, D., Mazelle, C., Eparvier, F.,
776 & Elrod, M. (2023). *MAVEN H⁻ Data (2014-2023)*. Zenodo. doi:
777 10.5281/zenodo.8422352
- 778 Henderson, S., Halekas, J., Lillis, R., & Elrod, M. (2021). Precipitating Solar Wind
779 Hydrogen as Observed by the MAVEN Spacecraft: Distribution as a Function
780 of Column Density, Altitude, and Solar Zenith Angle. *Journal of Geophysical*
781 *Research: Planets*, 126(7), e2020JE006725. (e2020JE006725 2020JE006725)
782 doi: <https://doi.org/10.1029/2020JE006725>
- 783 Holmström, M., Barabash, S., & Kallio, E. (2002). Energetic neutral atoms at Mars
784 1. Imaging of solar wind protons. *Journal of Geophysical Research: Space*
785 *Physics*, 107(A10). doi: <https://doi.org/10.1029/2001JA000325>
- 786 Huebner, W. F., Keady, J. J., & Lyon, S. P. (1992, September). Solar Photo Rates
787 for Planetary Atmospheres and Atmospheric Pollutants. , 195(1), 1-294. doi:
788 10.1007/BF00644558
- 789 Huebner, W. F., & Mukherjee, J. (2015, February). Photoionization and pho-
790 todissociation rates in solar and blackbody radiation fields. , 106, 11-45. doi:

- 791 10.1016/j.pss.2014.11.022
- 792 Hughes, A., Chaffin, M., Mierkiewicz, E., Deighan, J., Jain, S., Schneider, N., ...
- 793 Jakosky, B. (2019). Proton Aurora on Mars: A Dayside Phenomenon Perva-
- 794 sive in Southern Summer. *Journal of Geophysical Research: Space Physics*,
- 795 *124*(12), 10533-10548. doi: <https://doi.org/10.1029/2019JA027140>
- 796 Hughes, A., Chaffin, M., Mierkiewicz, E., Deighan, J., Jolitz, R., Kallio, E., ...
- 797 Hegyi, B. (2023). Advancing Our Understanding of Martian Proton Au-
- 798 rora through a Coordinated Multi-Model Comparison Campaign. *Journal of*
- 799 *Geophysical Research: Space Physics*.
- 800 Jakosky, B., Lin, R., & Grebowsky, J. e. a. (2015). The Mars Atmosphere and
- 801 Volatile Evolution (MAVEN) Mission. *Space Science Reviews*, *195*, 3-48. doi:
- 802 <https://doi.org/10.1007/s11214-015-0139-x>
- 803 Jones, N., Halekas, J., Girazian, Z., Mitchell, D., & Mazelle, C. (2022). MAVEN Ob-
- 804 servations of H^- Ions in the Martian Atmosphere. *Journal of Geophysical Re-*
- 805 *search: Planets*, *127*(6), e2021JE006999. (e2021JE006999 2021JE006999) doi:
- 806 <https://doi.org/10.1029/2021JE006999>
- 807 Kallio, E., & Barabash, S. (2000). On the elastic and inelastic collisions between
- 808 precipitating energetic hydrogen atoms and martian atmospheric neutrals.
- 809 *Journal of Geophysical Research: Space Physics*, *105*(A11), 24973-24996. doi:
- 810 <https://doi.org/10.1029/2000JA900077>
- 811 Kallio, E., & Barabash, S. (2001). Atmospheric effects of precipitating energetic
- 812 hydrogen atoms on the Martian atmosphere. *Journal of Geophysical Research:*
- 813 *Space Physics*, *106*(A1), 165-177. doi: <https://doi.org/10.1029/2000JA002003>
- 814 Kallio, E., Barabash, S., Brinkfeldt, K., Gunell, H., Holmström, M., Futaana, Y., ...
- 815 Dierker, C. (2006). Energetic Neutral Atoms (ENA) at Mars: Properties of
- 816 the hydrogen atoms produced upstream of the martian bow shock and impli-
- 817 cations for ENA sounding technique around non-magnetized planets. *Icarus*,
- 818 *182*(2), 448-463. (Results from the Mars Express ASPERA-3 Investigation)
- 819 doi: <https://doi.org/10.1016/j.icarus.2005.12.019>
- 820 Kallio, E., Luhmann, J. G., & Barabash, S. (1997). Charge exchange near Mars:
- 821 The solar wind absorption and energetic neutral atom production. *Journal of*
- 822 *Geophysical Research: Space Physics*, *102*(A10), 22183-22197. doi: <https://doi.org/10.1029/97JA01662>
- 823
- 824 Lewis, B., & Carver, J. (1983). Temperature dependence of the carbon dioxide pho-
- 825 toabsorption cross section between 1200 and 1970 Å. *Journal of Quantitative*
- 826 *Spectroscopy and Radiative Transfer*, *30*(4), 297-309. doi: [https://doi.org/10](https://doi.org/10.1016/0022-4073(83)90027-4)
- 827 [.1016/0022-4073\(83\)90027-4](https://doi.org/10.1016/0022-4073(83)90027-4)
- 828 Lindsay, B. G., Yu, W. S., & Stebbings, R. F. (2005, Mar). Cross sections for
- 829 charge-changing processes involving kilo-electron-volt H and H^+ with CO and
- 830 CO₂. *Phys. Rev. A*, *71*, 032705. doi: 10.1103/PhysRevA.71.032705
- 831 Mahaffy, P., Benna, M., & King, T. e. a. (2015). The Neutral Gas and Ion Mass
- 832 Spectrometer on the Mars Atmosphere and Volatile Evolution Mission. *Space*
- 833 *Science Reviews*, *195*, 49-73. doi: <https://doi.org/10.1007/s11214-014-0091-1>
- 834 Mahaffy, P. R., Benna, M., Elrod, M., Yelle, R. V., Bougher, S. W., Stone, S. W., &
- 835 Jakosky, B. M. (2015). Structure and composition of the neutral upper atmo-
- 836 sphere of Mars from the MAVEN NGIMS investigation. *Geophysical Research*
- 837 *Letters*, *42*(21), 8951-8957. doi: <https://doi.org/10.1002/2015GL065329>
- 838 McLaughlin, B. M., Stancil, P. C., Sadeghpour, H. R., & Forrey, R. C. (2017, may).
- 839 H photodetachment and radiative attachment for astrophysical applications.
- 840 *Journal of Physics B: Atomic, Molecular and Optical Physics*, *50*(11), 114001.
- 841 doi: 10.1088/1361-6455/aa6c1f
- 842 Mitchell, D., Mazelle, C., & Sauvaud, J. e. a. (2016). The MAVEN Solar Wind Elec-
- 843 tron Analyzer. *Space Science Reviews*, *200*, 495-528. doi: [https://doi.org/10](https://doi.org/10.1007/s11214-015-0232-1)
- 844 [.1007/s11214-015-0232-1](https://doi.org/10.1007/s11214-015-0232-1)
- 845 Mitchell, D. L., Lin, R. P., Mazelle, C., Rème, H., Cloutier, P. A., Connerney,

- 846 J. E. P., ... Ness, N. F. (2001). Probing Mars' crustal magnetic field and iono-
 847 sphere with the MGS Electron Reflectometer. *Journal of Geophysical Research:*
 848 *Planets*, 106(E10), 23419-23427. doi: <https://doi.org/10.1029/2000JE001435>
- 849 Nakai, Y., Shirai, T., Tabata, T., & Ito, R. (1987). Cross sections for charge
 850 transfer of hydrogen atoms and ions colliding with gaseous atoms and
 851 molecules. *Atomic Data and Nuclear Data Tables*, 37(1), 69-101. doi:
 852 [https://doi.org/10.1016/0092-640X\(87\)90005-2](https://doi.org/10.1016/0092-640X(87)90005-2)
- 853 Nier, A. O., & McElroy, M. B. (1977). Composition and structure of Mars' Upper
 854 atmosphere: Results from the neutral mass spectrometers on Viking 1 and
 855 2. *Journal of Geophysical Research (1896-1977)*, 82(28), 4341-4349. doi:
 856 <https://doi.org/10.1029/JS082i028p04341>
- 857 Parkinson, W., Rufus, J., & Yoshino, K. (2003). Absolute absorption cross
 858 section measurements of co₂ in the wavelength region 163–200 nm and
 859 the temperature dependence. *Chemical Physics*, 290(2), 251-256. doi:
 860 [https://doi.org/10.1016/S0301-0104\(03\)00146-0](https://doi.org/10.1016/S0301-0104(03)00146-0)
- 861 Rahman, F., & Hird, B. (1986). Electron detachment atomic cross sections from
 862 negative ions. *Atomic Data and Nuclear Data Tables*, 35(1), 123-183. doi:
 863 [https://doi.org/10.1016/0092-640X\(86\)90029-X](https://doi.org/10.1016/0092-640X(86)90029-X)
- 864 Ritter, B., Gérard, J.-C., Hubert, B., Rodriguez, L., & Montmessin, F. (2018). Ob-
 865 servations of the proton aurora on mars with spicam on board mars express.
 866 *Geophysical Research Letters*, 45(2), 612-619. doi: [https://doi.org/10.1002/](https://doi.org/10.1002/2017GL076235)
 867 [2017GL076235](https://doi.org/10.1002/2017GL076235)
- 868 Shematovich, V., & Bisikalo, D. (2021). A Kinetic Model for Precipitation of Solar-
 869 Wind Protons into the Martian Atmosphere. *Astronomy Reports*, 65, 869-875.
 870 doi: <https://doi.org/10.1134/S106377292110036X>
- 871 Shematovich, V. I., Bisikalo, D. V., Diéval, C., Barabash, S., Stenberg, G., Nilsson,
 872 H., ... Gérard, J.-C. (2011). Proton and hydrogen atom transport in the
 873 Martian upper atmosphere with an induced magnetic field. *Journal of Geo-*
 874 *physical Research: Space Physics*, 116(A11). doi: [https://doi.org/10.1029/](https://doi.org/10.1029/2011JA017007)
 875 [2011JA017007](https://doi.org/10.1029/2011JA017007)
- 876 Smith, S. J., & Burch, D. S. (1959, Feb). Photodetachment cross section of the neg-
 877 ative hydrogen ion. *Phys. Rev. Lett.*, 2, 165–166. doi: 10.1103/PhysRevLett.2
 878 .165
- 879 Stark, G., Yoshino, K., Smith, P., & Ito, K. (2007). Photoabsorption cross section
 880 measurements of co₂ between 106.1 and 118.7nm at 295 and 195k. *Journal of*
 881 *Quantitative Spectroscopy and Radiative Transfer*, 103(1), 67-73. doi: [https://](https://doi.org/10.1016/j.jqsrt.2006.07.001)
 882 doi.org/10.1016/j.jqsrt.2006.07.001
- 883 Stone, S. W., Yelle, R. V., Benna, M., Elrod, M. K., & Mahaffy, P. R. (2018).
 884 Thermal Structure of the Martian Upper Atmosphere From MAVEN
 885 NGIMS. *Journal of Geophysical Research: Planets*, 123(11), 2842-2867. doi:
 886 <https://doi.org/10.1029/2018JE005559>
- 887 Sun, H., & Weissler, G. L. (1955, 12). Absorption Cross Sections of Carbon Diox-
 888 ide and Carbon Monoxide in the Vacuum Ultraviolet. *The Journal of Chemical*
 889 *Physics*, 23(9), 1625-1628. doi: 10.1063/1.1742398
- 890 Wang, X.-D., Alho, M., Jarvinen, R., Kallio, E., Barabash, S., & Futaana, Y. (2018).
 891 Precipitation of Hydrogen Energetic Neutral Atoms at the Upper Atmosphere
 892 of Mars. *Journal of Geophysical Research: Space Physics*, 123(10), 8730-8748.
 893 doi: <https://doi.org/10.1029/2018JA025188>
- 894 Wang, X.-D., Barabash, S., Futaana, Y., Grigoriev, A., & Wurz, P. (2013). Direc-
 895 tionality and variability of energetic neutral hydrogen fluxes observed by Mars
 896 Express. *Journal of Geophysical Research: Space Physics*, 118(12), 7635-7642.
 897 doi: <https://doi.org/10.1002/2013JA018876>
- 898 Wishart, A. W. (1979, November). The bound-free photodetachment cross section of
 899 h-. *Journal of Physics B: Atomic and Molecular Physics*, 12(21), 3511. doi: 10
 900 .1088/0022-3700/12/21/009

901 Yoshino, K., Esmond, J., Sun, Y., Parkinson, W., Ito, K., & Matsui, T. (1996).
902 Absorption cross section measurements of carbon dioxide in the wave-
903 length region 118.7–175.5 nm and the temperature dependence. *Journal*
904 *of Quantitative Spectroscopy and Radiative Transfer*, 55(1), 53-60. doi:
905 [https://doi.org/10.1016/0022-4073\(95\)00135-2](https://doi.org/10.1016/0022-4073(95)00135-2)